

# Journal of Applied Remote Sensing

RemoteSensing.SPIEDigitalLibrary.org

## Monitoring of ground movement in open pit iron mines of Carajás Province (Amazon region) based on A-DInSAR techniques using TerraSAR-X data

Guilherme Gregório Silva  
José Claudio Mura  
Waldir Renato Paradella  
Fabio Furlan Gama  
Filipe Altoé Temporim

**SPIE.**

Guilherme Gregório Silva, José Claudio Mura, Waldir Renato Paradella, Fabio Furlan Gama, Filipe Altoé Temporim, "Monitoring of ground movement in open pit iron mines of Carajás Province (Amazon region) based on A-DInSAR techniques using TerraSAR-X data," *J. Appl. Remote Sens.* **11**(2), 026027 (2017), doi: 10.1117/1.JRS.11.026027.

# Monitoring of ground movement in open pit iron mines of Carajás Province (Amazon region) based on A-DInSAR techniques using TerraSAR-X data

Guilherme Gregório Silva, José Claudio Mura,\* Waldir Renato Paradella, Fabio Furlan Gama, and Filipe Altoé Temporim

National Institute for Space Research, São José dos Campos, São Paulo, Brazil

**Abstract.** Persistent scatterer interferometry (PSI) analysis of a large area is always a challenging task regarding the removal of the atmospheric phase component. This work presents an investigation of ground movement measurements based on a combination of differential SAR interferometry time-series (DTS) and PSI techniques, applied on a large area of extent with open pit iron mines located in Carajás (Brazilian Amazon Region), aiming at detecting linear and nonlinear ground movement. These mines have presented a history of instability, and surface monitoring measurements over sectors of the mines (pit walls) have been carried out based on ground-based radar and total station (prisms). Using *a priori* information regarding the topographic phase error and a phase displacement model derived from DTS, temporal phase unwrapping in the PSI processing and the removal of the atmospheric phases can be performed more efficiently. A set of 33 TerraSAR-X (TSX-1) images, acquired during the period from March 2012 to April 2013, was used to perform this investigation. The DTS analysis was carried out on a stack of multilook unwrapped interferograms using an extension of SVD to obtain the least-square solution. The height errors and deformation rates provided by the DTS approach were subtracted from the stack of interferograms to perform the PSI analysis. This procedure improved the capability of the PSI analysis for detecting high rates of deformation, as well as increased the numbers of point density of the final results. The proposed methodology showed good results for monitoring surface displacement in a large mining area, which is located in a rain forest environment, providing very useful information about the ground movement for planning and risk control. © The Authors. Published by SPIE under a Creative Commons Attribution 3.0 Unported License. Distribution or reproduction of this work in whole or in part requires full attribution of the original publication, including its DOI. [DOI: [10.1117/1.JRS.11.026027](https://doi.org/10.1117/1.JRS.11.026027)]

**Keywords:** DInSAR time-series; PSI; surface deformation; TerraSAR-X; open pit; Amazon region.

Paper 170102P received Feb. 3, 2017; accepted for publication May 15, 2017; published online Jun. 5, 2017.

## 1 Introduction

Carajás Mineral Province, located in the Brazilian Amazon region, encompasses the world's largest iron reserves with mining exploration carried out through open pit benching. Open pit operations usually have significant areas of extent with rock mass movements and surface displacements that potentially lead to slope instabilities with risks to personnel and equipment and affecting production. It is worth noting that small surface movements on a mine highwall may be a signal of a failure. Thus, a key concern for the mining industry is the prediction of mining-induced deformations of ground surface.

Taking advantage of multitemporal SAR acquisitions, the use of advanced differential SAR interferometry (A-DinSAR) techniques improves the capability for detecting deformation phenomena. A differential SAR interferometry (DInSAR) time-series (DTS) technique has been proposed and successfully used<sup>1-6</sup> and consolidated using the small baseline subset (SBAS)

---

\*Address all correspondence to: José Claudio Mura, E-mail: [mura@dpi.inpe.br](mailto:mura@dpi.inpe.br)

concept.<sup>7-11</sup> A persistent scatterer interferometry (PSI) approach<sup>12-15</sup> based on a stack of differential interferograms relies on identifying pixels whose scattering properties vary little with time and look angle, allowing a temporal analysis of the interferometric phase of individual point targets and providing accurate information related to the surface target displacements. PSI provides better spatial resolution and accuracy and can better model and diminish the effect of the atmospheric phase, which is related to the path delay heterogeneity during the acquisitions times, whereas the DTS technique can detect larger deformation rates and provides more homogeneous and extensive information related to the ground deformation, but at the cost of a loss in spatial resolution.

This paper is an outgrowth of the previous DInSAR investigations carried out with open pit iron mines in the Brazilian Amazon region.<sup>16-20</sup> This study presents an application of A-DInSAR techniques for monitoring surface deformation in a large area of extent with several open pit iron mines located in Carajás Mineral Province (Brazilian Amazon region). In the next section, a description of this particular mining area, as well as some related ground deformation instabilities, is presented. The combined approach based on DTS and PSI techniques using 33 StripMap TSX-1 scenes is presented in Sec. 3. The results of the combined techniques are presented in Sec. 4. The potential and the results of this approach for monitoring ground movement in a large mining area are discussed in Sec. 5. In Sec. 6, the validation is presented with topographic measurements (total station/prisms). The conclusion is given in Sec. 6.

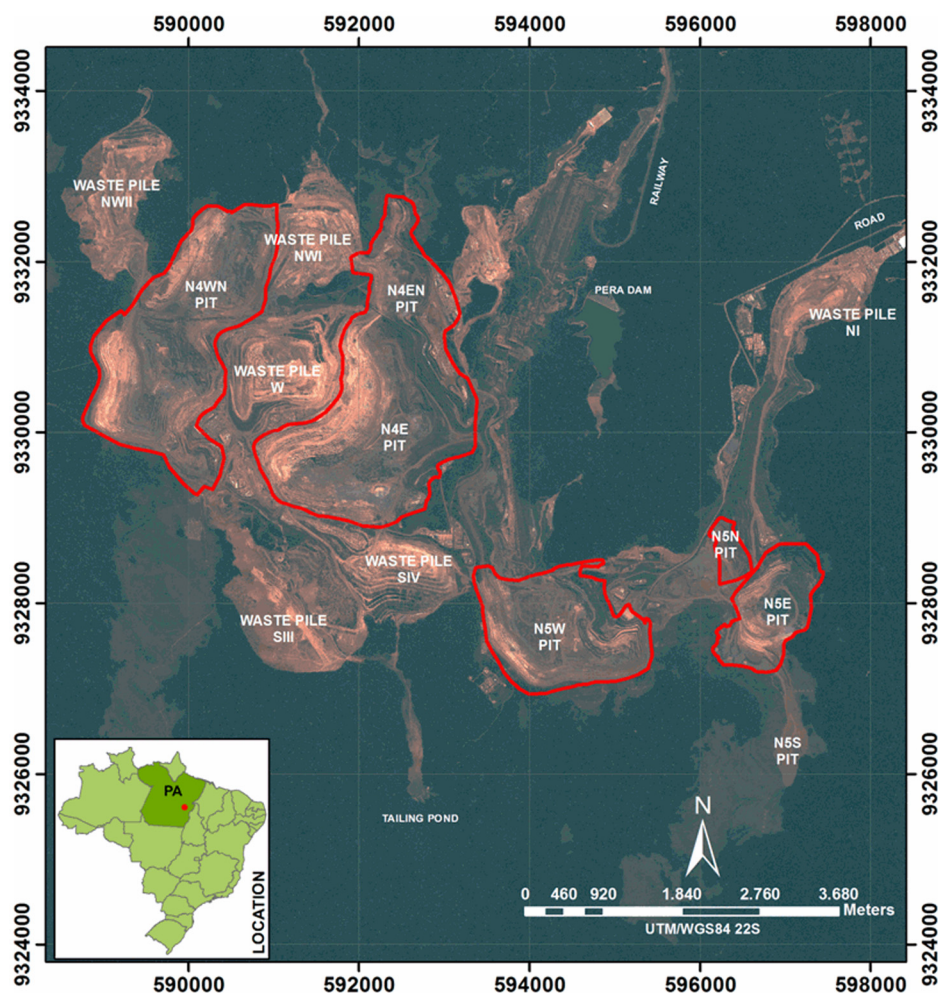


**Fig. 1** Location of Carajás iron complex in the Brazilian Amazon region (Pará State), showing the open pits, waste piles, and related mining infrastructures.

## 2 Study Area

The most important Brazilian mineral province is located in the Amazon Region, Carajás-PA, encompassing 39 iron bodies with reserves of 18 billion tons in an area of 120,000 km<sup>2</sup>. This province is marked by mountainous terrain, characterized by a set of hills and plateaus (altitudes from 500 to 900 m) surrounded by southern and northern lowlands (altitudes around 200 m), deep chemical weathering that produces thick oxisols (latosols), totally covered by ombrophilous equatorial forest communities with complex and multilevel canopies and numerous species.<sup>21</sup>

The iron deposits are covered by thick, hard iron-crust (lateritic duricrusts) developed over volcanic rocks and ironstones. Specific low-density savanna-type vegetation (campus rupestres) is associated with the deposits and shows a strong contrast (clearing) with the dense equatorial forest. Fully owned by Vale S.A. mining company, the exploration in Carajás is carried out through state-of-the-art open pit benching. The current mining activities are related to two iron ore bodies (N4 and N5) and started with the N4E mine in 1984 and with the N5W mine in 1998. Carajás Mining Complex (N4 and N5 bodies) (Fig. 1) produces ~300,000 metric tons of iron ore per day.<sup>17</sup>

Surface instabilities can be expected at any mining activity. Open pit operations usually have significant areas of extent and can also influence large portions of terrain adjacent to the pit crest. Rock mass movements and surface deformations potentially lead to slope instabilities or wall failures due to regular open pit mining operations. This scenario in Carajás gets worse over time due to intense deep excavations in saprolitic soil and rock masses of low geomechanical quality, coupled with blasting practices and heavy precipitation of the moist tropics, which has deleterious effects on the overall stability. Vale's geotechnical team has monitored the presence of fractures on bench walls and tension cracks on berms and road ramps through visual inspection, total station/reflecting prisms measurements, and ground-based radar.

## 3 Dataset

A stack with 33 TSX-1 StripMap images (repeat cycle of 11 days) was used in this investigation. Conflicts in acquisition programming of the satellite caused four interruptions in the original 1-year acquisition coverage starting on March 20, 2012, with four interruptions in 2012 (December 31) and 2013 (February 13, February 24, and March 7). The single look complex (SLC) images were acquired under ascending passes (look azimuth = 78 deg), with an incidence angle range of 39.89 to 42.21 deg, a spatial resolution of 1.7 m × 3.49 m (rg × az), pixel spacing of 1.36 × 1.90 m (rg × az), and a width swath of 30 km. To minimize the topography phase error in the interferometric process, a high-resolution DEM was produced based on a panchromatic GeoEye-1 stereo pair. The GeoEye stereo images were acquired over the study area on July 1, 2012. The first scene was collected with nominal azimuth and elevation angles of 29.4 deg and 82.4 deg, respectively, whereas the second scene was acquired with azimuth and elevation angles of 187.42 deg and 62.20 deg, respectively. The images were provided with 0.5-m spatial resolution and with rational polynomial coefficients. The generation of the DEM was based on OrthoEngine PCI Geomatics through the rational function method as the geometric model. The panchromatic DEM was produced using 2 m spacing, and its elevation values compared to seven well-defined accurate vertical check points have provided RMS and maximum errors of 1.2 and 1.6 m, respectively.<sup>22</sup>

## 4 Methodology

The proposed approach described in this paper is shown in Fig. 2, where the combination of two techniques, DTS and PSI, are used to improve the capability of the PSI technique for detecting nonlinear deformation, removal of the orbit phase trend error, and removal of the atmospheric phase delay in a large area, as well as increasing the numbers of point density of the final results. The deformation model and the DEM errors estimated by the DTS are subtracted from the master referenced differential interferogram, and the residual phases are processed with PSI technique.

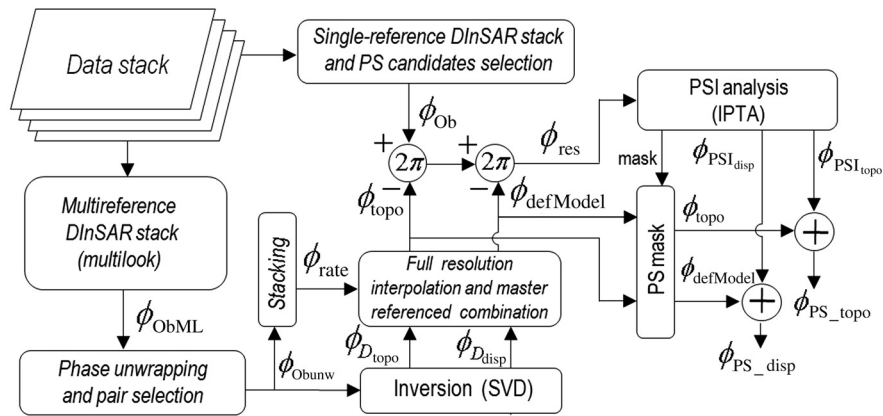


**Fig. 2** Flow diagram outlining the processing sequence of the proposed approach.

This approach was already applied to detecting nonlinear deformation in a small area of the Carajás Mineral Province.<sup>19</sup> In this work, we focus on the removal of the atmospheric phase component in a large area, where it is expected that it is not constant over the area.

#### 4.1 DTS Technique

The use of the standard DInSAR technique for monitoring surface deformation has been applied since the early '90s. DInSAR technique aims to measure deformation on the ground using a pair of SAR images acquired at different times and different positions of the satellite between two acquisitions. The interferogram generated from these two coregistered images has phase's component contributions from the topography, deformations, atmosphere, and noise. By knowing the positions of the satellite and the topographic surface, it is possible to subtract the topographic phase component and to measure the deformation. After removal of the phase component related to topography what remains in the differential interferogram is a contribution of the ground displacement between acquisitions added with other undesirable component, represented by

$$\varnothing_{\Delta t} = \varnothing_{\text{def}} + \varnothing_h + \varnothing_{\text{atm}} + \varnothing_{\beta} + \varnothing_n, \quad (1)$$

where  $\varnothing_{\text{def}}$  is the phase change due to the displacement of the pixel in the satellite line-of-sight (LoS) direction,  $\varnothing_h$  is the topographic phase error,  $\varnothing_{\text{atm}}$  is the atmospheric phase delay,  $\varnothing_{\beta}$  is the residual phase due to orbit errors, and  $\varnothing_n$  is the phase noise.

The ambiguity of  $2\pi$  in the differential interferometric phase (fringes) makes it impossible to interpret this phase in terms of absolute range change. However, it is possible to estimate the relative range change between points within a differential interferogram by integrating the number of fringes between them, using a process known as phase unwrapping.<sup>23</sup> Ground deformation monitoring is suitable when the  $\varnothing_{\text{def}}$  exceeds the other four phase components represented in Eq. (1). For this reason, the use of a precise DEM is desirable to compensate for part of the topographic phase error. A spatial filtering (multilook) can reduce the phase noise; however, the atmospheric phase delay and the residual phase due to orbit errors cannot be filtered out or estimated, respectively.

Taking advantage of multitemporal SAR acquisitions, the use of A-DinSAR techniques has improved the capability for detecting deformation phenomena. DTS and PSI algorithms have been developed to better address the standard DInSAR limitations using a redundant number of differential interferograms with the potential to determine spatially and temporally ground displacement, where the desirable deformation information can be separated from topography error, atmospheric delay, and noise.

Consider a set of  $M$  differential interferograms generated from a set of  $N + 1$  SAR images acquired at the ordered time  $(t_0, t_1, \dots, t_N)$ , where each differential interferometric pair is constructed in a given time interval  $(\Delta t)$ , as represented in Eq. (1), following the rule of small time interval between acquisitions or SBAS.<sup>7</sup> The observed multilook unwrapped phase values of this

point in relation to the reference point may be organized in a vector of  $M$  elements, represented by Eq. (2).

$$\varnothing_{MLOb}^T = [\varnothing_{\Delta t1}, \varnothing_{\Delta t2}, \dots, \varnothing_{\Delta tM}]. \quad (2)$$

Given  $N$  as the number of unknown phase values related to the range displacement of the selected point at the ordered time  $(t_1, t_2, \dots, t_N)$  and  $t_0$  as a reference epoch (zero deformation), the displacement vector can be represented by Eq. (3).

$$\varnothing_{disp}^T = [\varnothing_{\Delta r1}(t_1), \varnothing_{\Delta r2}(t_2), \dots, \varnothing_{\Delta rN}(t_N)]. \quad (3)$$

The relation between range displacement Eq. (3) and the observed data Eq. (2) can be represented as one system of  $M$  equation and  $N$  unknown variables in the matrix form in Eq. (4), where  $A$  is an  $M$  by  $N$  matrix of the operators  $(+1, -1, 0)$  between the unwrapped interferometric pairs.

$$A\varnothing_{disp} = \varnothing_{MLOb}. \quad (4)$$

The solution of Eq. (4) can be obtained in the least squares sense.<sup>2</sup> A physically sound solution can be found in terms of mean phase velocity among time-adjacent acquisitions using the SVD decomposition,<sup>7</sup> and a final integration can be used to achieve the final solution  $\phi_{Disp}$ .

The estimation of the topographic error ( $\phi_{Dtopo}$ ) can be determined by the coefficient of a linear regression that relates the topographic phase with the perpendicular baselines that compose the  $M$  interferograms, based on the following relation:

$$[\varnothing_{\partial h1}, \varnothing_{\partial h2}, \dots, \varnothing_{\partial hM}] = \frac{4\pi}{\lambda R \sin \theta} [B_{n1}, B_{n2}, \dots, B_{nM}], \quad (5)$$

where  $\lambda$  is the wavelength,  $R$  and  $\theta$  are the slant range distance and incidence angle of the master image used to coregister the stack of images, and  $B_n$  is the perpendicular baseline.

In this study, the inversion of the system of equation was performed using an extension of the SVD with a set of additional weighted constrain on the acceleration of the displacement to control the smoothness of the time-series solutions.<sup>3</sup> Temporal smoothing is enhanced using a finite difference approximation constraint, assuming that less deformation occurs during a short period of time. The smoothing constraint and the height error-related term were incorporated into the inversion of the system that relates the observed unwrapped interferograms phase with the average displacement velocity.<sup>24</sup>

A stack with 33 TSX-1 StripMap scenes was used to perform this investigation. It was planned to have one image every 11 days, but this sequence failed twice, creating discontinuities of 22 and 44 days. To cover the time span of acquisitions, it simulated the differential interferometric pairs for a time interval up to 45 days and a maximum perpendicular baseline up to 400 m (Fig. 3). Visual inspection was used to discard interferograms with compromising phase unwrapping errors. Most of the selected pairs belong to the shortest time interval among acquisitions (11 days).

The results of the DTS, ground displacement ( $\phi_{Ddisp}$ ) and topographic error ( $\phi_{Dtopo}$ ) are resampled for full resolution to have the same pixel spacing as that of the differential interferograms for the PSI analysis (Fig. 2). An important transformation is performed to change the phase displacement ( $\phi_{Ddisp}$ ) to the PSI phase model, which is referenced to the master image, as used in the PSI analysis, represented by

$$\varnothing_{DispModel}^T = \varnothing_{Disp}(t_1) - \varnothing_{Disp}(t_{Ma}), \varnothing_{Disp}(t_2) - \varnothing_{Disp}(t_{Ma}), \dots, \varnothing_{Disp}(t_N) - \varnothing_{Disp}(t_{Ma}). \quad (6)$$

The phase displacement model in Eq. (6) incorporates the phase rate (linear deformation) and the nonlinear deformation in relation to a reference point that is located in a stable area.

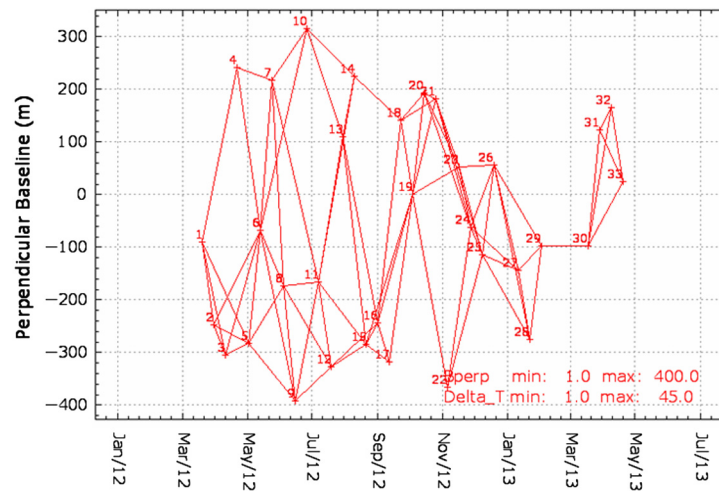


**Fig. 3** Interferometric pairs selected based on the stack of 33 TSX-1 images, with constraints on time interval of 45 days and perpendicular baseline of 400 m.

#### 4.2 PSI Technique

The PSI technique relies on identifying pixels whose scattering properties vary little with time and look angle in a stack of coregistered SLC images. The idea of PSI is to analyze the temporal and spatial characteristics of the interferometric phase of individual point targets. These point targets are coherent even for the interferometric pairs with long spatial baselines and remain stable over long time periods to permit analysis of the phase history.<sup>12–15</sup>

PSI analysis was carried out using the interferometric point target analysis (IPTA)<sup>14</sup> software, which is the implementation of PSI by GAMMA remote sensing and consulting AG (GAMMA). The IPTA software is a toolbox that can support many different methodologies including different alternatives for PS candidate selection, spatial and temporal phase unwrapping, and supporting approaches for single as well as multireferenced stacks; see Eq. (11). The processing sequence included SAR SLC image coregistration to generate the stack of interferograms (the master scene was selected based on a configuration that has low perpendicular baseline dispersion and is near to the center of the image sequence), the stack of differential interferograms generation, and the point target candidate determination (based on spectral phase diversity and low intensity variability). Figure 4 shows the flow diagram outlining the processing sequence for the PSI analysis using the IPTA technique shown in Fig. 3. The IPTA is based on a two-dimensional (2-D) regression (phase model indicating a linear dependence of the phase displacement with time and a linear dependence of the topographic phase with the perpendicular baseline). For the first regression to find the displacement rate, the best fit is found within the predefined parameters (maximum and minimum rate intervals) and the standard deviation bound of the regression; for the second regression, related to the estimation of the topographic error, the best fit is searched within the predefined height error interval. The regressions provide a set of layer (stack) of the unwrapped phase ( $\theta_{unw}$ ) and residual phase ( $\theta_{res}$ ), as well as single layers of the topographic phase error ( $\theta_{eh}$ ), the displacement rate ( $\theta_{rate}$ ), and the standard deviation of the linear regression fit of the displacement ( $\theta_{\sigma r}$ ). The model refinement shown in Fig. 4 presents several processing steps: phase unwrapping correction of layers with patch effect, baseline refinement, atmospheric phase removal from the spatially filtered residue, updating of the PS interferometric phase from estimated displacement rate, and the topographic phase error. In the last step, the residual atmospheric phase layers are checked for a new iteration. The computation of the linear and nonlinear displacement and the corrected digital elevation model are carried out after the last iteration.

In this analysis, 33 TSX-1 images acquired from March 2012 to April 2013 were used. The configuration of the interferometric pairs in relation to the master image (October 4, 2012) is shown in Fig. 5. PS candidates were estimated based on the amplitude dispersion index and low spectral diversity at each pixel of the stack of the coregistered images.<sup>13,14</sup> Considering the set of

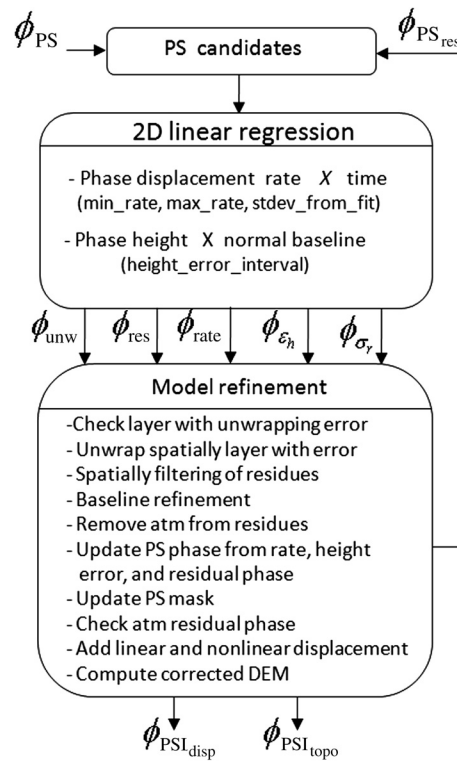


Fig. 4 Flow diagram of the processing sequence of the PSI analysis using IPTA methodology.

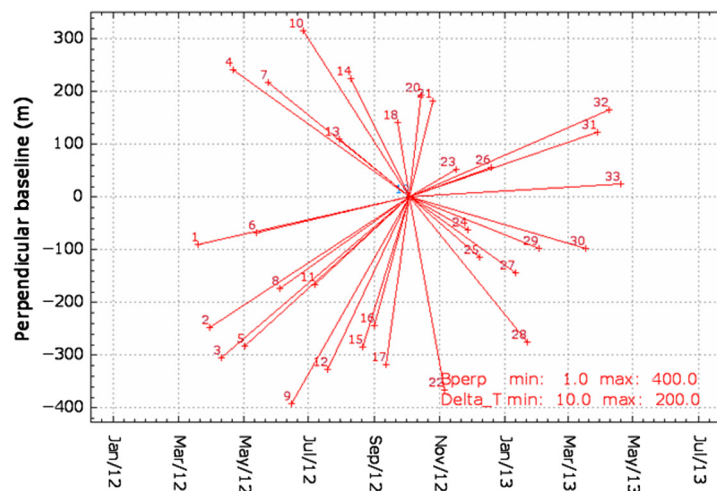


Fig. 5 Interferometric pairs in relation to the master image (October 4, 2012).

$N + 1$  SAR images acquired at the ordered time  $(t_0, t_1, \dots, t_N)$ , a reference point located in a stable area, and a selected generic PS, the observed wrapped phase values of this point in relation to the reference point can be organized in a vector of  $N$  elements as

$$\varnothing_{Ob}^T = [\varnothing_{\Delta t1}, \varnothing_{\Delta t2}, \dots, \varnothing_{\Delta tN}]. \quad (7)$$

The vector of wrapped phase represented in Eq. (7) has the components of deformation, topographic error, atmospheric artifacts, orbit errors, and noise. In this work, we propose using *a priori* knowledge of some phase components to improve the performance of the PSI analysis.

The results obtained from the DTS analysis, the topographic phase error  $\phi_{Dtopo}$ , and the phase deformation model  $\phi_{DispModel}$ , represented by Eq. (6), are subtracted from the observed phase

Eq. (7) to reduce the amount of these phase components, aiming at improving the PSI analysis with IPTA. The phase  $\phi_{D_{\text{Topo}}}$  is subtracted (module- $2\pi$ ) from the observed phase vector Eq. (7), resulting in the first residual wrapped phase, which is then subtracted (module- $2\pi$ ) from the phase displacement model, as shown in Fig. 2, resulting in a residual wrapped phase represented in Eq. (8), which is used as input phase for the PSI analysis represented in Fig. 4.

$$\phi_{\text{res}}^T = \phi_{\text{Ob}}^T - \phi_{\text{Topo}}^T - \phi_{\text{Disp Model}}^T \quad (8)$$

The residual phase represented in Eq. (8) presents the atmospheric phase component, orbits phase error, phase noise, and residual phase due to the errors occurred during the DTS processing in the estimation of the topographic error, as well as errors related to the phase model in Eq. (6), which contain the components of the linear and nonlinear deformation. Considering that the larger phase components (topography error and linear and nonlinear ground displacement) have been removed in Eq. (8), the PSI processing can better performed the removal of the atmospheric phase and noise, improving the determination of the final ground displacement.

Performing PSI analysis for a large area is always a challenging task regarding the removal of the atmospheric phase component. An important aspect of the IPTA technique is the possibility of a stepwise, iterative improvement for different parameters to estimate the topographic error, atmospheric phase delay, and ground displacement. The residue layers of the linear regression related to the displacement can present phase unwrapping errors, including the patch effect due to the local reference used. To overcome this problem, the layers with phase unwrapping error are transformed to a complex format filtered spatially and afterward unwrapped again until all layers have been unwrapped properly. This processing step can be repeated until a suitable box size for the filter is found.

In this work, three iterations were performed to improve the estimation of the ground displacement and the removal of the atmospheric phase components. A new iteration is decided based on the statistics of the residual atmospheric phase of all layers. The atmospheric phase component may account for the most of the linear regression deviation (residues) related to the linear deformation, considering that the larger phase components related to the linear and nonlinear movement and topographic error have been removed previously from the DTS results. The spatial statistics of the atmospheric residual phase for all layers presented a range of values from 0.5 up to 5.1 rad, 0.3 up to 0.8 rad, and 0.3 up to 0.7 rad for the three iterations, respectively. Figure 6 shows the estimated atmospheric phase component (in module) for one layer composed by the images master (October 4, 2012) and slave (October 28, 2012) in three iterations. It can be noted in Fig. 6 that, after the second iteration, the residual phase remains very low.

The final solution for the deformation was obtained by adding the PSI result to the DTS phase displacement model, represented by Eq. (9), and for the final topographic error by the addition of the components from PSI analysis with the DTS, as represented in Eq. (10). Only the PS present in the PS\_mask (Fig. 2) was validated.

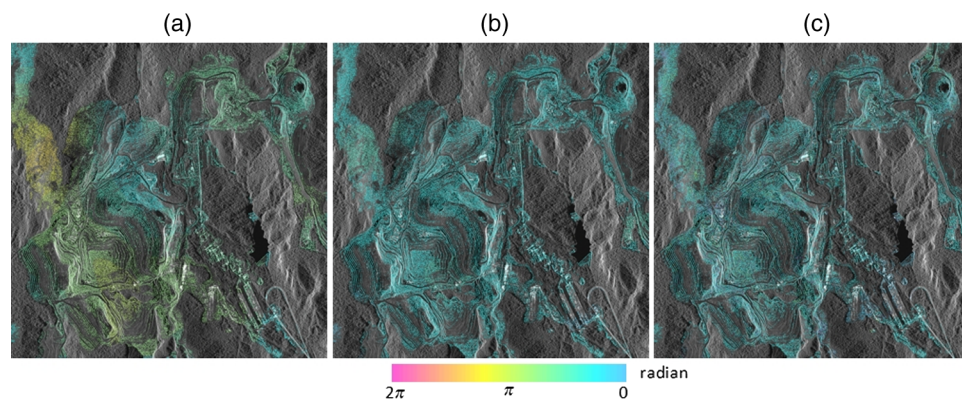


**Fig. 6** Atmospheric residual phase components obtained after the (a) first iteration, (b) second iteration, and (c) third iteration for the pair of images acquired on October 4, 2012 (master) and October 28, 2012.

$$\varnothing_{\text{PSdisp}}^T = \varnothing_{\text{PSI disp}}^T + \varnothing_{\text{Disp Model}}^T, \quad (9)$$

$$\varnothing_{\text{PS topo}}^T = \varnothing_{\text{PSI topo}}^T + \varnothing_{\text{D topo}}^T. \quad (10)$$

## 5 Results and Discussion

The ground displacement map obtained with the proposed methodology, using 33 TSX-1 scenes and covering the time span from March 2012 to April 2013 (dry and wet seasons), is shown in Fig. 7. PSI processing, using previous information about the phase displacement model and DEM error derived from the DTS, allows the detection of ground movement in a large area, covering the complex of the N4 and N5 open pit iron mines (Fig. 1).

No relevant ground displacement was found around and within the pits and mining infrastructures (green-bluish regions, Fig. 7). However, high deformation rates (yellow-reddish regions, Fig. 7) with negative values corresponding to motion away from the satellite were detected over the waste piles corresponding to the letters A, B and C (Fig. 7). Furthermore, it was also possible to detect evidence of deformation over the slopes of the N5W mine (letter D, Fig. 7). For the waste piles, the detected displacement was interpreted as related to settlements, showing values normally expected for this manmade structure. On the other hand, lithostructural and lithogeomechanical attributes played a key role in the displacements related to the cut slopes in N5W. The maximum accumulated displacements (along the LoS and away from the satellite) were  $-78$  cm (waste pile NW-1, letter A),  $-61$  cm (waste pile W, letter B),  $-46$  cm (waste pile S-IV, letter C), and  $-34$  cm (cut slopes of N5W, letter D).

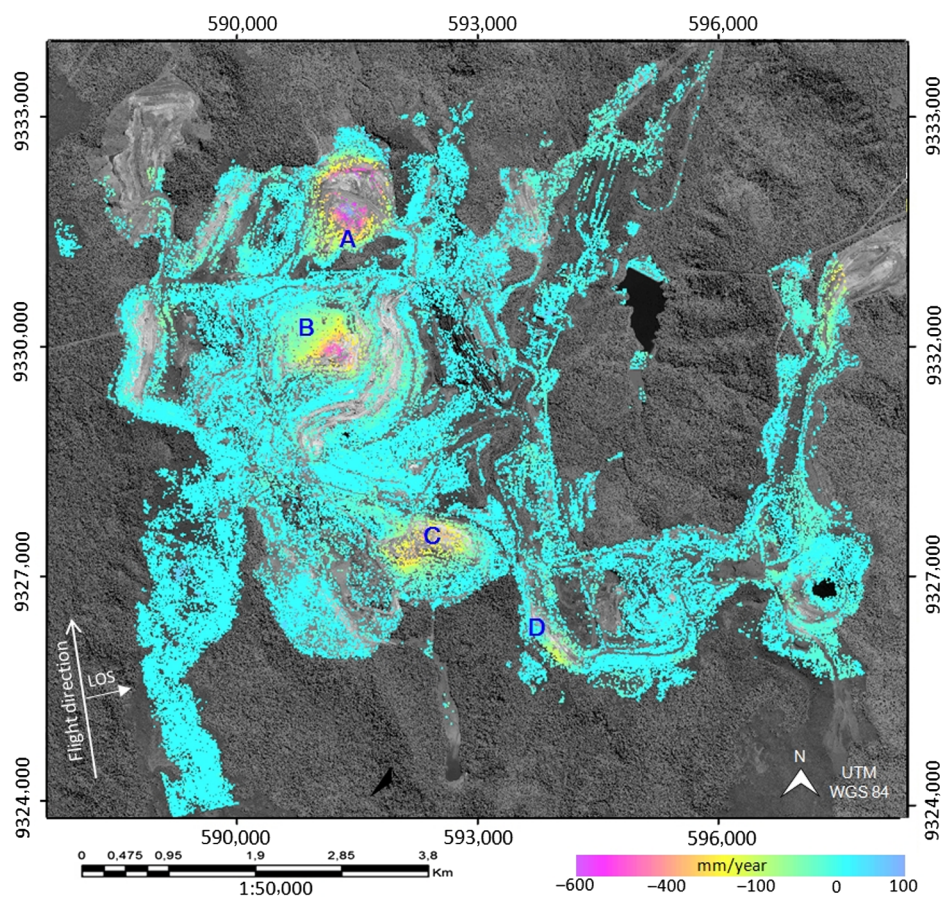


**Fig. 7** Ground displacement map expressed by the average LoS velocity from March 2012 to April 2013 based on 33 TSX-1 scenes.

Differential interferometric measurements shown in Fig. 7 were carried out with respect to a reference point that was selected within the area of interest, assumed as stable, and time referenced to the acquisition date of the first scene. Therefore, displacements data provided for PS are relative, not absolute, data. The accuracy of these measurements can be estimated through the dispersion of PS values regarding the reference point, expressed by the standard deviation of the displacement rate, represented according to Gamma<sup>25</sup> by

$$\sigma_{Vd(x,r)} = \sqrt{\sum_{i=1}^N \left( \frac{\lambda}{\Delta t_i 4\pi} \phi_{PS\text{disp}(i)} - \frac{\lambda}{4\pi} \phi_{PS\text{rate}} \Delta t_i \right)^2 / \Delta t_i^2}, \quad (11)$$

where

$$\phi_{PS\text{rate}} = \sum_{i=1}^N \Delta t_i \phi_{PS\text{disp}(i)} / \sum_{i=1}^N \Delta t_i^2, \quad (12)$$

where  $\phi_{PS\text{disp}(i)}$  is the phase displacement of a PS during the time interval  $\Delta t_i$  and  $N$  is the number of interferograms.

Figure 8 shows the standard deviation map of the average displacement rates for the 33 images processed using the proposed methodology.

Geomechanical classes and the corresponding deformation rates on the ore bodies (Fig. 1) are shown in Fig. 9 for the N4W and N4E mines. It can be noticed from Fig. 9, for both mines, that the more relevant ground displacements are related to the poor and very poor geomechanical classes. This shows that, apart from the mining activity, poor geomechanical characteristics have played a key role in the displacement process. Table 1 reveals some relationships of PS and geomechanical classes for the mines N4W and N4E, showing that the highest amount of detected

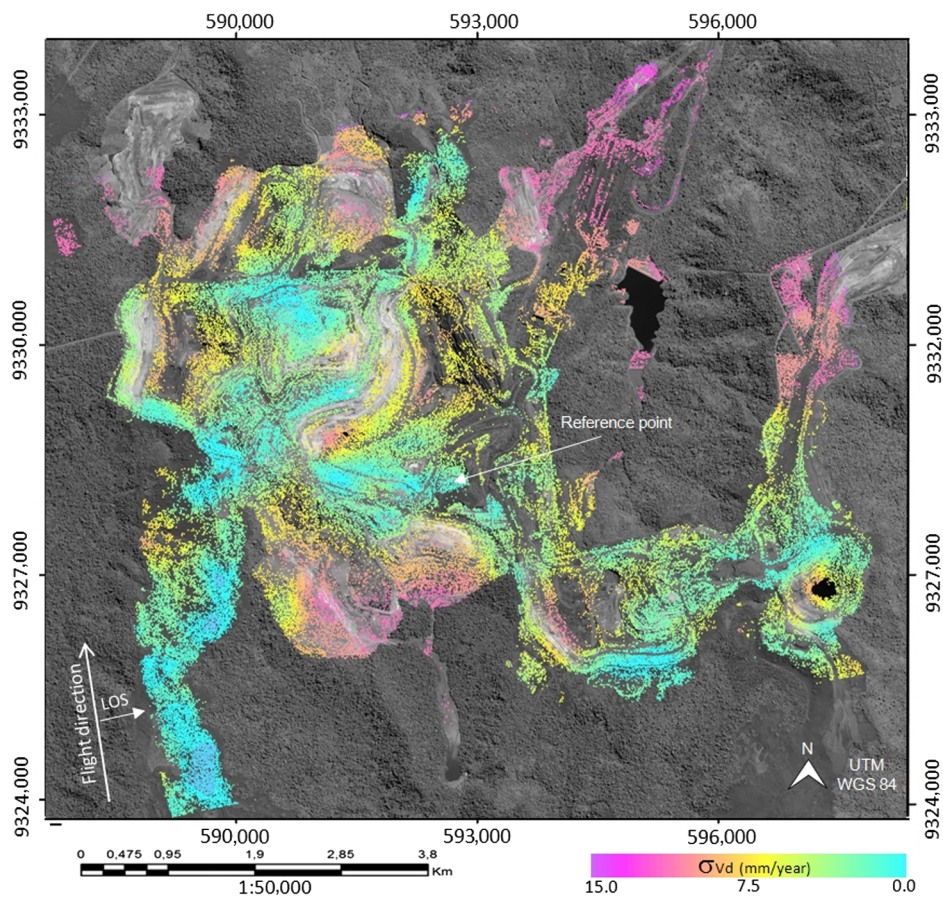
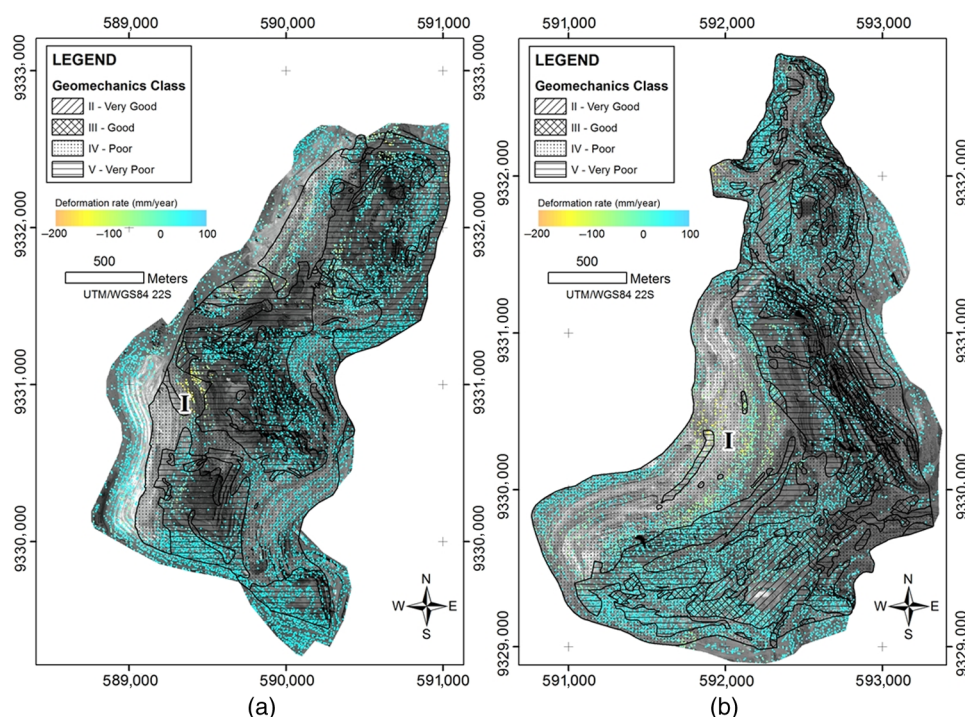


Fig. 8 Standard deviation map of the average displacement rates.



**Fig. 9** Deformation rate and geomechanical classes of the (a) N4W and (b) N4E mines.

**Table 1** Relationship between PS and geomechanical classes for the N4W and N4E mines.

Geomechanical class	Mine					
	N4W			N4E		
	Area (km <sup>2</sup> )	Number of PS	PS/km <sup>2</sup>	Area (km <sup>2</sup> )	Number of PS	PS/km <sup>2</sup>
Very good	0.05315	110	2070	0.428628	1132	2641
Good	0.02281	47	2109	0.349786	904	2584
Poor	1.30733	2310	1767	2.701338	5152	1907
Very poor	2.13865	3433	1605	1.214203	2739	2256

PS was associated with geomechanical classes with the largest areas but presenting the lowest densities (classes IV and V). These two classes present geomechanical attributes of poor quality and the most intense exploitation activities.

Figure 10 shows the geomechanical classes and the deformation rates on the ore bodies corresponding to the N5W and N5E mines. For both mines, the more relevant ground displacements are related to the poor and very poor geomechanical classes. The relationships between PS and geomechanical classes shown in Table 2 for the mine N5W reveal that the highest amount of detected PS was associated with the largest areas, corresponding to the very poor geomechanical class and reaching displacement rate value up to  $-34$  mm/year on the cut slope. This displacement was validated with prism measurements, as discussed in the validation section. For the mine N5E, Table 2 reveals that the poor geomechanical class has the highest area and number of PS, with the high density for all classes, probably due to the low activities in this mine.

In an attempt to validate the results of the proposed approach with field information, a set of measurement points using total station/prisms was used for the validation purpose. To make representative comparisons, the vertical prism measurement data were converted to the LoS of the TSX-1 satellite. The conversion was performed by multiplying the prism measurements

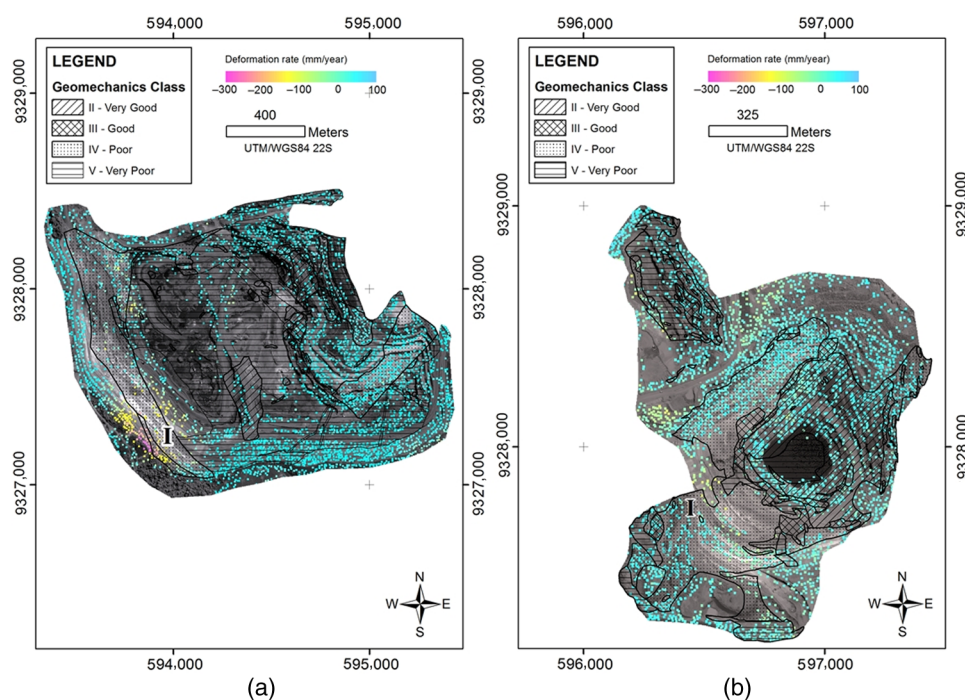


**Fig. 10** Deformation rate and geomechanical classes of the (a) N5W and (b) N5E mines.

**Table 2** Relationship between PS and geomechanical classes for N5W and N5E mines.

Geomechanical class	Mine					
	N5W			N5E		
	Area (km <sup>2</sup> )	Number of PS	PS/km <sup>2</sup>	Area (km <sup>2</sup> )	Number of PS	PS/km <sup>2</sup>
Very good	0.103060	90	873	0.231646	635	2741
Good	0.021535	53	2461	0.067126	170	2533
Poor	0.405898	756	1863	0.414293	968	2337
Very poor	1.141563	1754	1536	0.189917	330	1738

by the cosine of the incidence angle ( $\theta \approx 41$  deg). With the purpose of ensuring that the values obtained by both interferometric and prism measurement refer to the same place, only the closest data pairs were selected. The available field data are related to six sites located along cut slopes of the NW-1 waste pile. These slopes are constituted of highly weathered metavolcanic rocks.<sup>26</sup> Figure 11 shows the PSI displacement map, the prism positions, and the related displacement measurements of both techniques. It can be noted that for the period of June to September of 2012 there is an agreement among the different measurements techniques for the six prisms, even considering the prism measurements with a high variability (probably due to variations of total station position of human operation during the measurements), showing any distinguishable deformation trend, which indicates that the slope cuts were stable during the time span. This result was also confirmed by the local geotechnical team of Vale S.A. mining company.

During the period of TSX-1 acquisitions, the slopes of the N5W mine were monitored with total station/prisms. The available prism measurements from April 24, 2012, up to September 28, 2012, were compared with PSI results at the acquisition date from May 3, 2012, up to October 4, 2012, every 11 days, as shown in Fig. 12. The choice of the PS was based on the nearest neighbor of the measured point belonging to the same slope; a weighted average instead could use the PS

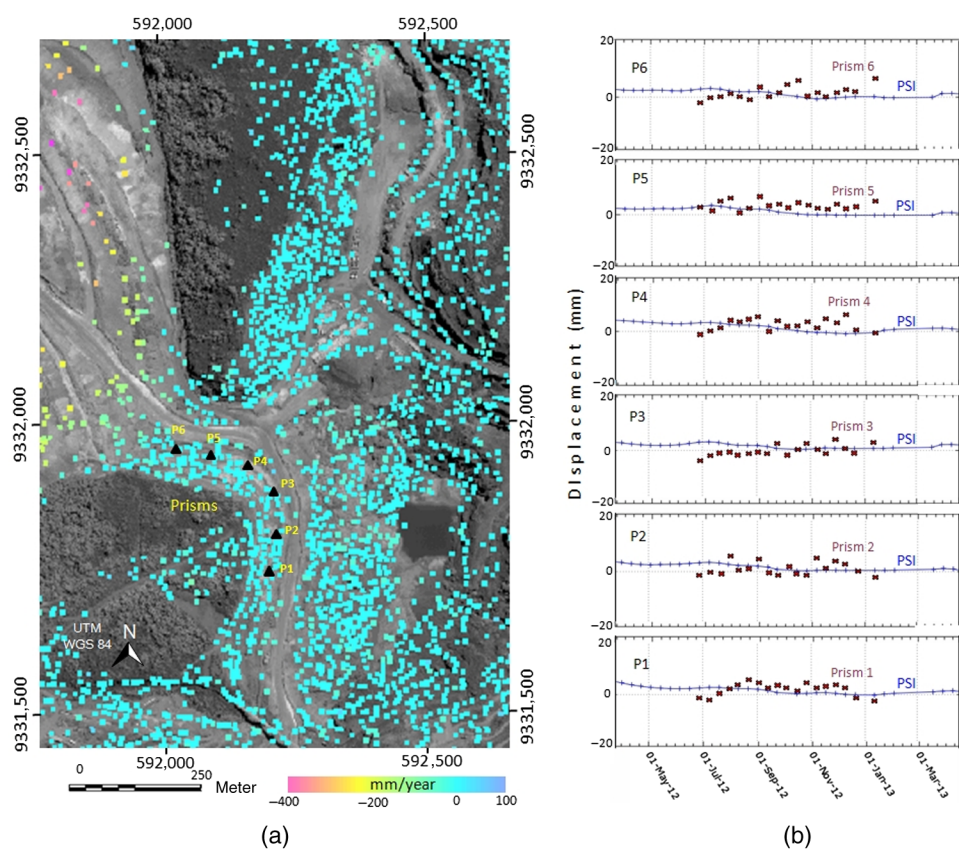


**Fig. 11** (a) Ground displacement map with six prisms positions and (b) related graphs of displacement history for both techniques.

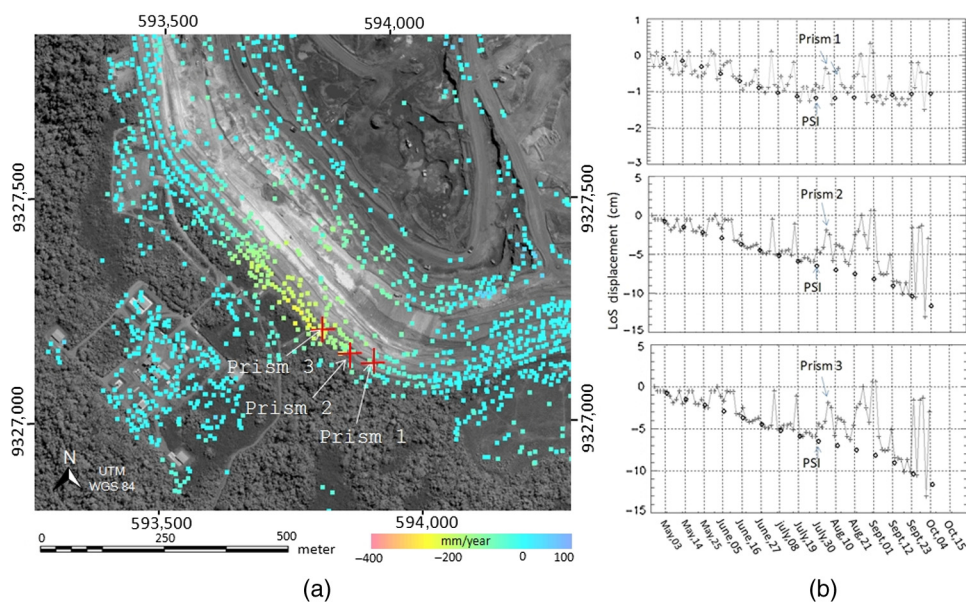


**Fig. 12** (a) Ground displacement map (LoS direction) of the slopes of N5W with prisms locations obtained from March 2012 to April 2013 and (b) the related displacement graphs (from May 3, 2012, up to October 4, 2012) for both techniques.

belonging to different slopes, contaminating the slope displacement itself. The distances from the prism position to the nearest neighbor PS were 1.9, 4.1, and 3.4 m for the prism 1, prism 2, and prism3, respectively.

Topographic measurements by total station/prisms have a high variability [Fig. 12(b)], probably due to the positioning of the total station at each measurement. The computed error between the PSI and prism measurements provided the following results: mean difference equal to 0.085, 1.19 and 1.29 cm for the prisms 1, 2, and 3, respectively, and RMSE of 0.25, 2.29, and 1.95 cm for the prisms 1, 2, and 3, respectively. Even considering these errors, there is a good agreement with PS displacements in terms of trend for the three prism locations.

## 6 Conclusions

The proposed methodology took advantage of the previous knowledge and removal of the two more markedly phase components (ground displacement and topographic error) provided by DTS processing; thus, the atmospheric residual phase, orbit refinement, phase noise, and the remaining phase related to the ground displacement and topographic error could be determined more efficiently with the PSI analysis, based on the IPTA technique, making the processing of large areas of extent easier.

The combination of DTS and PSI techniques together with high-resolution TerraSAR-X data, acquired at relatively short intervals (11 day) and covering the time span from March 2012 to April 2013, allowed the detection of linear and nonlinear deformations on the overall mining area. The main affected sectors were the waste piles, reaching accumulated values up to  $-78$  cm, as with the case of the NW-1 waste pile (Fig. 1) (letter A, Fig. 7). Another sector affected by ground displacement was the cut slopes of N5W (letter D in Fig. 7), reaching accumulated values up to  $-34$  cm. Deep excavations in rock masses of low geomechanical quality coupled with blasting practices and heavy precipitation contributed to this ground displacement. This work presented a methodology that can be applied to monitoring linear and nonlinear ground displacements in a large extent mining area, providing spatial coverage and useful information about ground movement for mining planning and risk assessment.

## Acknowledgments

This investigation was carried out under the scope of an FAPESP-Vale-INPE project (Process FAPESP # 2010/51267-9). The Coordination of Improvement of Higher Education Personnel (CAPES) and the National Council for Scientific and Technological Development (CNPq) are also recognized for a donation received by the first, third, and fifth authors, respectively, during the investigation. The authors would like to thank Vale S.A. for providing access to geological and geomechanical information. Finally, the authors are particularly grateful to the Geotechnical Vale team in Carajás for the support during the field work campaign.

## References

1. P. Lundgren et al., "Modeling surface deformation observed with SAR interferometry at Campi Flegrei caldera," *J. Geophys. Res.* **106**, 19355 (2001).
2. S. Usai, "A least-squares approach for long-term monitoring of deformations with differential SAR interferometry," in *Proc. Geoscience and Remote Sensing Symp. (IGARSS '02)*, Vol. 2, Toronto, Ontario, Canada, pp. 1247–1250 (2002).
3. D. A. Schmidt and R. Bürgmann, "Time-dependent land uplift and subsidence in the Santa Clara valley, California from a large InSAR data set," *J. Geophys. Res.* **108**(B9), 2416–2429 (2003).
4. O. Mora, J. J. Mallorquí, and A. Broquetas, "Linear and nonlinear terrain deformation maps from a reduced set of interferometric SAR images," *IEEE Trans. Geosci. Remote Sens.* **41**(10), 2243–2253 (2003).
5. M. Crosetto, B. Crippa, and E. Biescas, "Early detection and in-depth analysis of deformation phenomena by radar interferometry," *Eng. Geol.* **79**, 81–91 (2005).

6. A. H. Ng et al., "Mapping accumulated mine subsidence using small stack of SAR differential interferograms in the southern coalfield of New South Wales, Australia," *Eng. Geol.* **115**, 1–15 (2010).
7. P. Berardino et al., "A new algorithm for surface deformation monitoring based on small baseline differential SAR interferograms," *IEEE Trans. Geosci. Remote Sens.* **40**(11), 2375–2383 (2002).
8. R. Lanari et al., "A small-baseline approach for investigating deformations on full-resolution differential SAR interferograms," *IEEE Trans. Geosci. Remote Sens.* **42**(7), 1377–1386 (2004).
9. C. Lee et al., "Deformation of the Augustine Volcano, Alaska, 1992–2005, measured by ERS and ENVISAT SAR interferometry," *Earth Planets Space* **60**, 447–452 (2008).
10. L. Jiang et al., "Potential of small-baseline SAR interferometry for monitoring land subsidence related to underground coal fires: Wuda (Northern China) case study," *Remote Sens. Environ.* **115**, 257–268 (2011).
11. S. Samsonov and N. D'Oreye, "Multidimensional time-series analysis of ground deformation from multiple InSAR data sets applied to Virunga Volcanic Province," *Geophys. J. Int.* **191**, 1095–1108 (2012).
12. A. Ferretti, C. Prati, and F. Rocca, "Nonlinear subsidence rate estimation using permanent scatterers in differential SAR interferometry," *IEEE Trans. Geosci. Remote Sens.* **38**(5), 2202–2212 (2000).
13. A. Ferretti, C. Prati, and F. Rocca, "Permanent scatterers in SAR interferometry," *IEEE Trans. Geosci. Remote Sens.* **39**(1), 8–20 (2001).
14. C. Werner et al., "Interferometric point target analysis for deformation mapping," in *Proc. of the IEEE Int. Geoscience and Remote Sensing Symp. (IGARSS '03)*, Toulouse, Vol. 7, pp. 4362–4364 (2003).
15. A. Hooper et al., "A new method for measuring deformation on volcanoes and other natural terrains using InSAR persistent scatterers," *Geophys. Res. Lett.* **31**, L23611 (2004).
16. M. E. Hartwig, W. R. Paradella, and J. C. Mura, "Detection and monitoring of surface motions in active open pit iron mine in the Amazon region; using persistent scatterer interferometry with TerraSAR-X satellite data," *Remote Sens.* **5**, 4719–4734 (2013).
17. J. C. Mura et al., "Monitoring of surface deformation in open pit mine using DInSAR time-series: a case study in the N5W iron mine (Carajás, Brazil) using TerraSAR-X data," *Proc. SPIE* **9243**, 924311 (2014).
18. W. R. Paradella et al., "Mapping surface deformation in open pit iron mines of Carajás Province (Amazon region) using an integrated SAR analysis," *Eng. Geol.* **193**, 61–78 (2015).
19. C. A. Pinto et al., "Applying persistent scatterer interferometry for surface displacement mapping in the Azul open pit manganese mine (Amazon region) with TerraSAR-X data," *J. Appl. Remote Sens.* **9**, 095978 (2015).
20. J. C. Mura et al., "Monitoring of non linear ground movement in an open pit iron mine based on an integration of advanced DInSAR techniques using TerraSAR-X data," *Remote Sens.* **8**, 409 (2016).
21. W. R. Paradella et al., "A geobotanical approach to the tropical rain forest environment of the Carajás Mineral Province (Amazon region, Brazil), based on digital TM-Landsat and DEM data," *Int. J. Remote Sens.* **15**(8), 1633–1648 (1994).
22. W. R. Paradella and P. Cheng, "Using GeoEye-1 stereo data in mining applications: automatic DEM generation," *Geoinformatics* **16**, 10–12 (2013).
23. M. Constantini, "A novel phase-unwrapping algorithm based on network programming," *IEEE Trans. Geosci. Remote Sens.* **36**(3), 813–821 (1998).
24. L. C. Werner, U. Wegmueller, and T. Strozzi, "Deformation time-series of the lost-hills oil field using a multi-baseline interferometric SAR inversion algorithm with finite difference smoothing constrains," in *AGU Fall Meeting* (2012).
25. Gamma Remote Sensing, "User's guide version 1.4," in *GAMMA Remote Sensing and Consulting AG*, Bern, Switzerland (2013).
26. W. Daynes, "Vale Brazil—Carajás iron ore mine - by Will Daynes (business excellence-January 30, 2013)," <http://www.republicofmining.com/2013/01/31/vale-brazil-carajas-iron-ore-mine-bywill-daynes-business-excellence-january-30-2013> (25 May 2017).

**Guilherme Gregório Silva** is an environmental engineer. He graduated in environmental engineering from the University of Vale do Paraíba, Brazil, in 2010, and his MS degree in remote sensing from INPE, in 2017. His research interests include topography, cartography, geodesy, environment, remote sensing, GIS, SAR classification, and interferometry.

**José Claudio Mura** received his BS degree in electric engineering from the University of São Paulo (USP) at São Carlos School of Engineering, Brazil, in 1978, his MS degree in electronics and telecommunications from the Aeronautics Institute of Technology, Brazil, in 1985, and his PhD in applied computer science from INPE, in 2000. He has been with INPE since 1979 and his current research interests include SAR image processing, SAR polarimetry, and interferometry.

**Waldir Renato Paradella** is a geologist with a BS degree in geology from the USP, Brazil, in 1973, MS degree in remote sensing from INPE, in 1976, and PhD in geology from the USP, in 1983. Since 1974, he has been with INPE and currently is a senior researcher. In 1988 and 1995, he was with CCRS, Canada, as a postdoctoral fellow and visiting scientist. His main research interests include geoscience applications in tropical environments with SAR.

**Fabio Furlan Gama** graduated in electronic engineering from Vale do Paraíba University, São José dos Campos, Brazil, in 1986, and received his MS and PhD degrees in remote sensing from INPE, in 1996 and 2007, respectively. He currently works at INPE as a senior researcher in the Image Processing Department in development and applications of SAR polarimetry and interferometry. Currently, he is working in estimation of surface deformation using advanced differential interferometric techniques.

**Filipe Altoé Temporim** graduated in geology from the Universidade Federal do Espírito, in 2014 and received his MS degree in remote sensing from INPE, in 2017. His main research interests include geoscience applications using SAR data and SAR interferometry in mining applications.